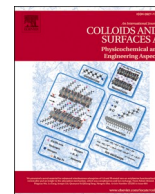




Contents lists available at ScienceDirect

Colloids and Surfaces A: Physicochemical and Engineering Aspects

journal homepage: www.elsevier.com/locate/colsurfa

Size-tunable graphitized carbon spheres for water defluoridation

B.V.N. Sewwandi^a, A.R. Kumarasinghe^{a,e}, Z. Wu^{b,d}, P.M.C.J. Bandara^{b,d}, L. Jayarathne^b, Athula Bandara^b, Himal Wijekoon^b, Xing CHEN^{b,c,*}, Rohan Weerasooriya^{b,c,*}

^a Department of Physics, Faculty of Applied Sciences, University of Sri Jayewardenepura, Nugegoda, Sri Lanka

^b Centre for Water Quality Research, National Institute of Fundamental Studies, Kandy, Sri Lanka

^c Key Lab of Aerospace Structural Parts Forming Technology and Equipment of Anhui Province, Institute of Industry and Equipment Technology, Hefei University of Technology, Hefei 230009, PR China

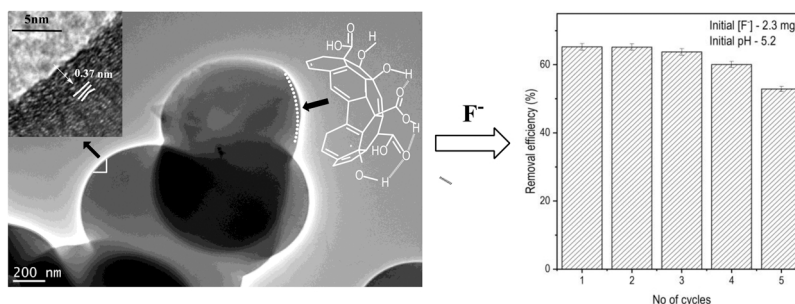
^d Postgraduate Institute of Science, University of Peradeniya, Peradeniya, Sri Lanka

^e Center for Nanocomposite Research, Faculty of Applied Sciences, University of Sri Jayewardenepura, Nugegoda, Sri Lanka

HIGHLIGHTS

- Single step non-catalytic chemical vapor deposition method is used for the fabrication of carbon spheres.
- Size tunability of the carbon spheres is achieved by modulating $C_2H_2:N_2$ flow ratios.
- A formation mechanism of carbon spheres is proposed based on spectral signatures and molecular dynamics simulations.
- Carbon spheres show an enhanced ability to remove fluoride in drinking water upon repeated use for five cycles.

GRAPHICAL ABSTRACT



ARTICLE INFO

Keywords:

Non-catalytic carbon spheres
Chemical vapor deposition
Hierarchical morphology
Size controllability
Fluoride absorption

ABSTRACT

We fabricated non-catalytic carbon spheres with controllable dimensions (diameter 0.3–1.5 μm) by chemical vapour deposition at 1273 K using C_2H_2 (carbon source) and N_2 (dilutant) gas precursors. By varying the flow rates of precursor gases, spherical or pseudo-spherical morphologies with chain-like hierarchical structures are discerned. The X-ray diffraction data show hexagonally graphitized networks. The mechanism of carbon sphere formation is not yet fully resolved largely due to the ambiguity associated with the nucleation step, viz. pentagon or heptagon route. According to molecular dynamics calculations, the formation of carbon pentagons is energetically more favorable than heptagons. Pentagon structures seem to form by closing Fjord regions of the graphitized network as evidenced in IR bands at 635 cm^{-1} and 796 cm^{-1} . The X-ray photon spectroscopic (XPS) measurements show adventitious oxygen on the carbon sphere's surface sites with $-COOH$ and $-C-C=O$ groups. The $-COOH$ and $-C-C=O$ groups are polar; hence, the carbon spheres' surface sites readily hydroxylate (where $\equiv GOH^{\delta}$ represents surface sites with a fractional charge). The carbon sphere synthesized under $\left(\frac{C_2H_2}{N_2}\right) = \frac{5}{6}$ gas flow ratio (viz., CS3) shows the highest fluoride removal capacity, viz., $0.095 \pm 0.01\text{ mmol.m}^{-2}$. The comparable

* Corresponding authors at: Centre for Water Quality Research, National Institute of Fundamental Studies, Kandy, Sri Lanka.

E-mail addresses: bnsewwandi1@gmail.com (B.V.N. Sewwandi), argk@sjp.ac.lk (A.R. Kumarasinghe), wuzhi@chinhangroup.com (Z. Wu), jayanibandara93@gmail.com (P.M.C.J. Bandara), lakmal.ja@nifs.ac.lk (L. Jayarathne), athulatbandara@yahoo.com (A. Bandara), himal.shankana@gmail.com (H. Wijekoon), xingchen@hfut.edu.cn (X. CHEN), rohan.we@nifs.ac.lk (R. Weerasooriya).

<https://doi.org/10.1016/j.colsurfa.2023.131582>

Received 15 February 2023; Received in revised form 30 April 2023; Accepted 1 May 2023

Available online 2 May 2023

0927-7757/© 2023 Elsevier B.V. All rights reserved.

zeta potential values observed between the carbon spheres and fluoride laden carbon spheres point to an anion exchange of surface hydroxyl ions for F^- sorption. In agreement with the XPS data, the broad IR band at 3440 cm^{-1} due to H-bonded surface hydroxyl stretching vibrations has resolved into three discrete bands, e.g., 3640 , 3752 , and 3738 cm^{-1} , which evidenced fluoride adsorption. Compared to activated carbon, the retention of fluoride on carbon spheres is over 60 times higher, which shows its potential in water treatment in removing fluoride.

1. Introduction

Over 200 million people worldwide are exposed to drinking water with high fluoride [1,2]. Fluoride is a biologically active element that requires regulation within a narrow concentration window between 1.00 and 1.50 mg/L to ensure good dental and bone health [3]. Long-term exposure to excessive fluoride can also damage DNA and induces cancer [4–6]. However, people in the tropics consume large quantities of water, resulting in high fluoride intake. Hence the WHO guidelines for drinking water may require modifications depending on specific country requirements [7].

Various water defluoridation methods such as precipitation, membrane-based electro-dialysis processes, and adsorption are available [8,9]. Methods based on precipitation or adsorption generate excess wastes that require additional attention. Membrane methods such as reverse osmosis remove virtually all solutes in water, rendering them unpalatable [10].

Carbon-derived materials have peculiar solute-sieving properties that can be used in the water treatment industry [11,12]. However, the application of graphene oxide (GO), reduced graphene oxide (rGO), or carbon nanotubes (CNT) in the water industry shows limitations due to their high production cost and ecotoxicity [13–16]. The topology of the carbon atomic network seems to relate to their toxicity [17]. In contrast, the carbon spheres show biocompatibility and low toxicity [18–20]. On the other hand, activated carbon is widely used in the water industry to remove taste, odor, turbidity, and color; however, it contains a haphazard pore network that yields disjoint channels and voids showing water flow resistance. Further, controlling the structural properties of activated carbon such as porosity, surface chemistry, and specific surface area is challenging [7,21]. In contrast, due to spherical morphology, carbon sphere-derived materials can be used in the water treatment industry in place of activated carbon. When hydroxylated, the trapping capacity of contaminants by carbon sphere is enhanced due to the abundance of surface sites [22], variable specific surface area [23], and favorable surface charging [24–26]. Carbon spheres or their functionalized variants have applications in diverse fields such as water treatment [24,26], rechargeable batteries [27], electronic devices fabrication [28,29], medicine [30], catalyst carrier [28], and supercapacitors [31], to name a few.

The carbon spheres (CS) can be fabricated by arc-discharge process, laser ablation, autoclave methodology [23,32], mixed-valence oxide catalytic [33], and high-pressure carbonization [34,35]. However, these methods show limitations largely due to specialized technology used and hazardous waste generation [36]. Although environmentally benign, chemical vapor deposition (CVD) methods are not widely used for CS fabrication [37]. This technology has several variants: catalytic CVD [38–41], non-catalytic CVD [42–44], or template CVD [45]. Out of these methods, the non-catalytic CVD technique is promising in fabricating carbon spheres, particularly due to the following reasons; a. CS can be fabricated in a single step without a catalyst, b. the CVD methods are well screened from intimate human involvements, c. waste gaseous by-products generated in the CVD reactor zone can safely be removed by airflow, [46] d. gaseous reactants (presently C_2H_2 in N_2 carrier) are safer than liquid /solid-state chemicals, e. the surfaces of carbon spheres are smooth and the pores can easily be tunable [42,47] f. high CS production throughput at a low cost showing its potential for scaling up in industrial applications [48].

The non-catalytic CVD method is used to fabricate tunable carbon spheres by changing system parameters, e.g., temperature, gas flow rate, carbon source, and templates [43,48,49]. A tunable carbon sphere (size range $200\text{--}500\text{ nm}$) was fabricated by acetylene pyrolysis at $1000\text{ }^\circ\text{C}$ under a nitrogen atmosphere using a vertical non-catalytic CVD reactor [50]. Further, the ball and chain-like tunable carbon spheres were produced using toluene at various carrier gas flow rates [42]. When a liquid hydrocarbon is used as a carbon source, a two-step CVD is required to synthesize carbon spheres. But only in a few cases, carbon spheres were fabricated via a non-catalytic route without paying much attention to their morphology based on growth parameters (e.g., precursor gas flow rate, materials template, etc.) [42,43,51]. In any case, the mechanistic steps of the carbon sphere growth on different templates also required identification.

The conversion of C_2H_2 into benzene on a red-hot Fe, Cu, or quartz tube (e.g., 873 K) is well known. Thus, acetylene pyrolysis occurs on the solid surface or in the gas phase [52]. Several reactors were used to examine acetylene pyrolysis, and flow reactors are appropriate when the temperature varies between 900 and 2500 K [53,54]. Thus, hydrogen, methane, vinylacetylene, benzene, naphthalene, and ethylene are mainly formed by direct acetylene pyrolysis [53–57]. Further, acetylene-mediated polycyclic aromatic hydrocarbon (PAH) growth occurs through the hydrogen abstraction C_2H_2 addition (HACA) mechanism forming a carbon sphere with different morphologies [53,54, 57–60]. Various structural configurations of the graphitic flakes have initiated carbon sphere nucleation resulting in spherical C-derived moieties. On the surface of these graphitic flakes, carbon ring structures of different configurations tend to accumulate [61]. Compared to other C-derived materials, the chemistry of carbon spheres strongly depends on the reactions of open edges along graphitic flakes. The unclosed fractions of carbon rings on the carbon sphere surface possess reactive dangling bonds, making them suitable for adsorption [61,62]. As a result, when interacting with water the carbon spheres' surface is already functionalized with C-OH, C=O, and C-OOH hydrophilic groups [50]. The density of these groups can enhance with NaOH or toluene/ethanol treatment [25,26]. Heteroatomic doping such as S doped-carbon spheres can also enhance the sorption ability of surface sites [23,63].

In this research, we synthesized high-purity carbon spheres by non-catalytic CVD route using acetylene precursor in a nitrogen atmosphere. The success of CS applications in various fields depends on their tunable propensity. We attained the CS size tunability by varying inlet $\left(\frac{C_2H_2}{N_2}\right)$ gas flow ratios at a specified temperature. The carbon sphere morphology and other surface properties were characterized using scanning and transmission microscopy, molecular spectroscopy, and x-ray photon spectroscopy. Besides, the effect of the precursor gas flow rates on the carbon spheres morphology and the growth mechanism was also examined. Past research identifying precise mechanism for the formation of carbon spheres is daunting due to the uncertainty associated with the nucleation step of coiling up graphitic structures [43,48, 61]. We attempted to resolve this ambiguity using spectroscopic observations coupled with molecular dynamics simulations. We also selected biologically active fluoride as an index ion to illustrate the role of carbon spheres in drinking water treatment at the pre-treatment step.

2. Experimental

2.1. Materials

Analytical grade methanol and acetone were received from Sigma Aldrich (USA). Sodium fluoride was from Fluke (Switzerland). Ultra-pure water was used in all experiments.

2.2. Carbon spheres synthesis

A CVD furnace containing a horizontal ceramic tube (heating zone: 75 mm ID and 900 mm length) was used to synthesize carbon spheres (Kejia, PR China). The gas flow of the CVD can be controlled at $\pm 1.0 \text{ cm}^3 \text{ STP/min}$ resolution. The ceramic boat was symmetrically mounted on the ceramic tube and placed in a programmable oven at the desired temperature. The oven temperature was ramped at $10^\circ \text{C} \cdot \text{min}^{-1}$ under nitrogen gas (purity 99.99%) purging. Then the production of carbon spheres, named as CS1, CS2, CS3, CS4, and CS5 (hereafter CS, $x = 1-5$), was initiated using $\left(\frac{\text{C}_2\text{H}_2}{\text{N}_2}\right)$ gas flow ratios at $\frac{1}{10}$, $\frac{3}{8}$, $\frac{5}{6}$, $\frac{7}{4}$, and $\frac{9}{2}$, respectively for 1 h (refer to Table 2-S for gas mass flow rates). The supply of C_2H_2 was then stopped and the N_2 supply was continued until the reactor cooled down to ambient room temperature.

2.3. CSx ($x = 1-5$) characterization

The crystallographic structures of CSx ($x = 1-5$) were examined by X-ray diffraction spectroscopic patterns (XRD) obtained at a scanning speed of 4° min^{-1} , and 2θ ranges from 10° to 60° (Rigaku Ultima IV Cu-K α radiation, $\lambda = 0.154056 \text{ nm}$, Japan). Here crystal sizes of CSx ($x = 1-5$) were calculated by combined Debye-Scherrer (Eqs. 2 to 4) and Bragg's (Eq. 1) equations to determine the d_{002} values of each sphere:

$$n\lambda = 2d\sin\theta \quad (1)$$

(Where d is the distance between atomic planes in the crystalline phase, the wavelength of X rays, λ)

$$L_c = \frac{0.94\lambda}{\beta_c \cos\theta} \quad (2)$$

$$L_a = \frac{1.84\lambda}{\beta_a \cos\theta} \quad (3)$$

$$N = \frac{L_c}{d_{002}} + 1 \quad (4)$$

(The interplanar spacing (d) of the sample is calculated while the stacking height (L_c), the stacking layer length (L_a), and the number of layers (N) of the crystallites).

The CSx ($x = 1-5$) surface morphology and microstructures were determined by scanning electron microscopy (SEM ZEISS EVO 40 SE detector, Germany) and transmission electron microscopy (TEM, JEM-1400flash, Japan). Near-surface elemental composition and functional groups of the materials were examined by X-ray photoelectron spectroscopy (ESCALAB250Xi Thermo, USA). The IR spectra of CSx ($x = 1-5$) were collected using a Fourier transform infrared (FTIR) spectrometer (Thermo Nicolet, S10, USA). A Raman spectrometer scanned Raman spectra (Thermo Nicolet DXR, USA). The specific surface area, pore size and pore volume of the CS samples were determined using Brunauer–Emmett–Teller (BET) analyzer (Autosorb IQ3 USA). The proton and hydroxyl exchange of carbon spheres' surfaces was also estimated by proton titrations of the particulates' suspension in 0.01 M NaNO_3 at 298 K under continuous N_2 purging by an auto titrator (KEM AT-610, Japan). The pH 4.01 ± 0.01 , 7.00 ± 0.01 , and 10.01 ± 0.02 buffers (Thermo fisher scientific, USA) were used in the pH electrode calibration. The fluoride concentrations of the solution were measured

by a fluoride ion-selective electrode (Metrohm 6.0502.150) using an automatic titrator (Metrohm Titrand 907, Switzerland).

2.4. Fluoride adsorption by CSx ($x = 1-5$)

The fluoride removal by $0.15 \pm 0.01 \text{ g/L}$ CSx ($x = 1-5$) was determined using a simulated water sample with the composition: pH 5.20 ± 0.01 , 2.30 mg/L fluorides. The CSx ($x = 1-5$) was hydroxylated with 0.01 M NaOH. Based on the highest fluoride adsorption, the CS3 sample was chosen for further studies. Fluoride adsorption isotherm for CS3 was constructed at 298 K using the following initial conditions; F 39 – 526 μM (mg/L 0.75–10.0), CS3 $0.15 \pm 0.01 \text{ g/L}$, pH 5.2 ± 0.01 . The 25 mL of fluoride and CS3 suspensions were equilibrated in 50 mL centrifuge tubes using an end-to-end shaker (MS-RD-Pro Rotor, HINOTEK China). The particulate separation from the solution was carried out using 0.22 μm syringe filters. The supernatant and 0.094 mol/dm $^{-3}$ HOAc/ 0.005 mol/dm $^{-3}$ NaOAc buffer solutions were mixed at a 1:1 ratio to determine the total fluoride activity by the standard addition method. The z-core for proficiency assessment of fluoride measurements ranges between 0.00 and 0.41. The fluoride removal efficiency by CSx ($x = 1-5$) was determined as follows:

$$\text{Fluoride removal Efficiency} = \frac{[F^-]_{\text{initial}} - [F^-]_{\text{final}}}{[F^-]_{\text{initial}}} \times 100 \quad (1)$$

2.5. Fluoride adsorption kinetics by CS3 and reusability

The chemical kinetics of fluoride adsorption by CS3 was examined using a 500 mL batch reactor containing 2.00 mg/L F^- and 0.15 $\pm 0.01 \text{ g/L}$ CS3 at pH 5.20 ± 0.01 in 0.01 M NaCl at 298 K (viz., $\left(\frac{[\text{GOH}]}{[\text{F}^-]}\right) \gg 1$). The preparative details of the batch suspension are given in Section 2.4. At predefined time intervals, 1.0 mL of the suspension aliquots were filtered through 0.45 μm membranes for residual fluoride analysis in decant solution.

The efficiency of fluoride removal by CS3 after repeated use of the substrate was also measured. A $0.15 \pm 0.01 \text{ g}$ CS3 was reacted with 2.30 mg. L $^{-1}$ fluoride solution at pH 5.20 ± 0.01 in 0.01 M NaCl for 12 h. The fluoride-laden CS3 was washed rapidly with 0.01 M NaOH for 10 min and re-utilized for fluoride adsorption experiments for five cycles. The fluoride removal efficiency at each cycle was calculated by the method shown in Eq. (1) by accounting for the slight mass lost during the regeneration step.

2.6. Molecular dynamics simulations

The geometry optimization of the plausible carbon ring structures (except aromatic rings) was carried out by extensive molecular dynamics (MD) simulations with a large-scale atomic molecular massively parallel simulator (LAMMPS) [64]. The Adaptive Intermolecular Reactive Empirical Bond Order (AIREBO) [65] force field of accounting for interatomic interactions between C-C and C-H (Support documentation, Fig. 1-S). Our simulation domain was periodic in all directions. Initially, the total energy of a given carbon cyclic structure was minimized using the conjugate gradient method and further relaxed for 5 ns under the canonical (NVT) ensemble. A time step of 0.5 fs was used for all the simulations. The details of the calculations are shown in support documentation (Fig. 1-S and Table 1-S).

3. Results and discussion

3.1. Size controllable non-catalytic carbon spheres

We fabricated carbon spheres (CSx) by a non-catalytic route using C_2H_2 (C source) and N_2 (dilutant) precursor gases at 1273 K and 1 atm

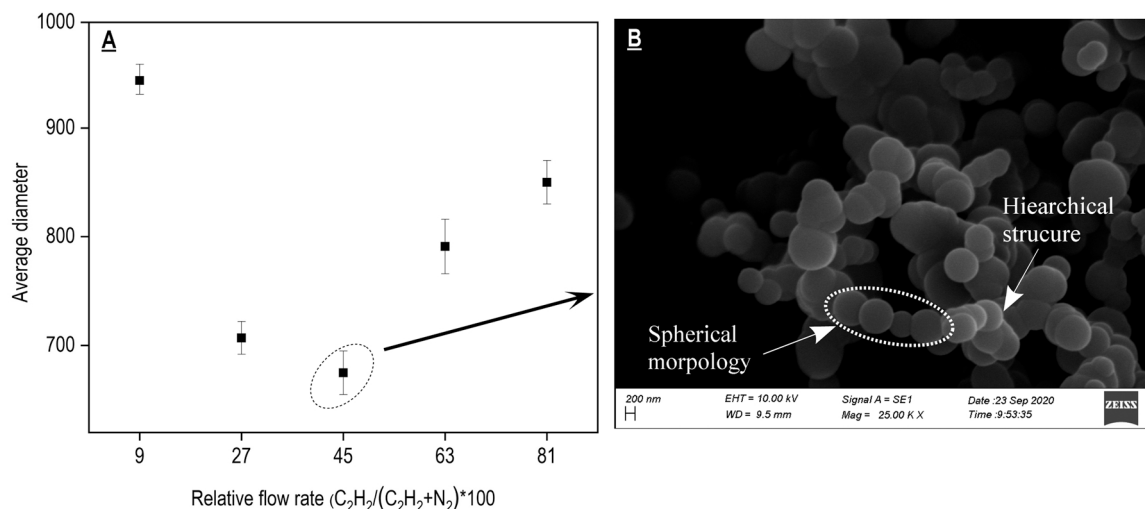


Fig. 1. **A.** Variation of the average diameter of CS_x ($x = 1-5$) as a function of $\% \left(\frac{C_2H_2}{C_2H_2+N_2} \right)$. Error bars \pm sd. A minimum dimension of around 675 ± 20 nm is observed at % 45 relative flow rates, **B.** SEM of minimized CS3 (e.g., 45% relative flow rates). Spherical shapes and hierarchal CS3 micro-structures are common.

(viz. CS_x, $x = 1-5$). As shown in the SEM data (Fig. 2S a - e, supporting documentation), irrespective of the variations of inlet $\left(\frac{C_2H_2}{N_2} \right)$ gas flow ratios, the CS_x ($x = 1-5$) always retained a spherical or pseudo-spherical morphology with a well-defined hierarchical structure (Fig. 1B). The $\left(\frac{C_2H_2}{N_2} \right)$ gas flow ratio determines the critical size of the carbon spheres [53], resulting in a minimal dimension (e.g., 675 nm) at 45% relative gas flow rate, viz., $\left(\frac{C_2H_2}{C_2H_2+N_2} \right)$ (Fig. 1A).

We also observed hierarchal CS structures on various regions of the CVD machine via gas-phase C vapor nucleation followed by heterogeneous particulate growth [66] (Fig. 2S. a-e). The layering of carbon nuclei by carbon vapors results in a spherical structure; the cohesion of two such proximal structures results in dumbbell shape particulates. By repeating the CS cohesion process, hierarchal CS structures result in both low (e.g., 9%) or high (e.g., 80%) $\left(\frac{C_2H_2}{C_2H_2+N_2} \right)$ relative flow rates (Fig. 1a & b) [50,67]. At high N₂ flow rates, viz., N₂ > 600 cm³ STP/min, most of the C₂H₂ and other carbonaceous remnants flushed away from the CVD reactor without forming carbon spheres [38,68]. Carbon sphere formation is fast, and its relative density is high. At high gas flow ratios, intense collisions lead to carbon sphere agglomeration. Distorted CS_x ($x = 1-5$) with large dimensions thus results in high and low C₂H₂ flow rates (Fig. 2S: a- e).

3.2. XRD and TEM measurements of CS_x ($x = 1-5$)

We used XRD and TEM data to determine the carbon spheres' growth morphology as a function of the relative gas flow ratio [69]. The CS_x ($x = 1-5$) shows poor graphitization (Fig. 2A). All XRD profiles are monotonous, showing broad peaks around $2\theta \sim 24.34^\circ$, 24.82° and $\sim 43.39^\circ$ - 43.55° respectively, which correspond to (002) and (100) graphitic planes. Fig. 2B shows the variation of interlayer spacing (d_{002}) as a function of the carbon sphere size.

The carbon sphere below 675 nm dimension results in stacking small graphitic flakes (6.17 nm²) (Table 3S). The defects required for layer stacking are created during nucleation by the edge dislocations and twinning [70] (Fig. 3b). The CS3 has the lowest stacking length, L_c (1.49 nm), and height, L_a (4.14 nm) (Table 3S). Further, the carbon spheres start neck growth which results in ordered graphitic layer packing. As shown in Fig. 2S and Table 3S, when pentagonal-heptagonal pairs are dominant, large carbon spheres result from the regular stacking of parallel graphitic flakes. The relevant data for CS1 and CS3 are shown in Fig. 3.

We used XRD and TEM data to estimate the stacking distance of carbon layers. The interlayer stacking distance of CS3 (e.g., 0.37 nm) is larger than CS1 (e.g., 0.36 nm), implying the role of graphitic flakes on the carbon sphere size (Fig. 2B). The nanostructured features for the carbon spheres are obtained by transmission emission microscopic

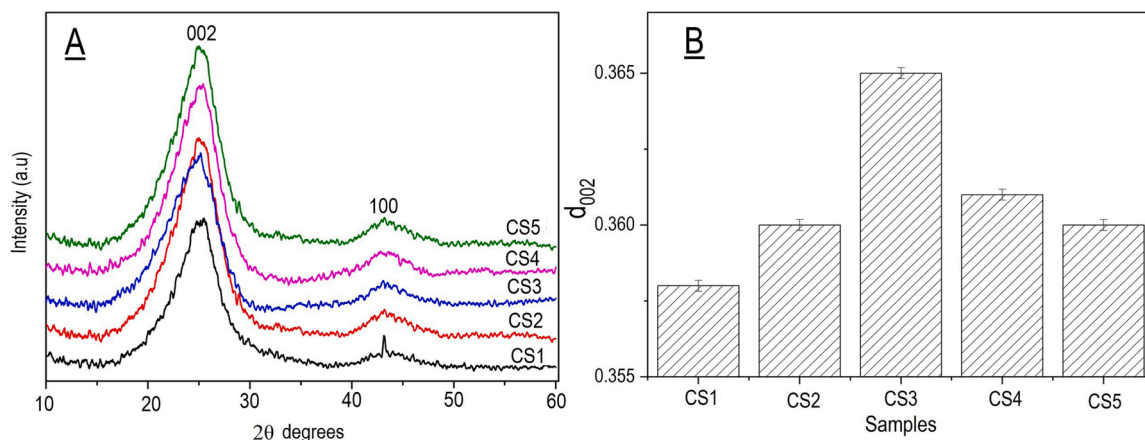


Fig. 2. **A.** XRD patterns of CS_x ($x = 1-5$) samples. **B.** Interlayer distance (d_{002}) variation of CS_x ($x = 1-5$) samples. error bars \pm 0.05% (Table 3S).

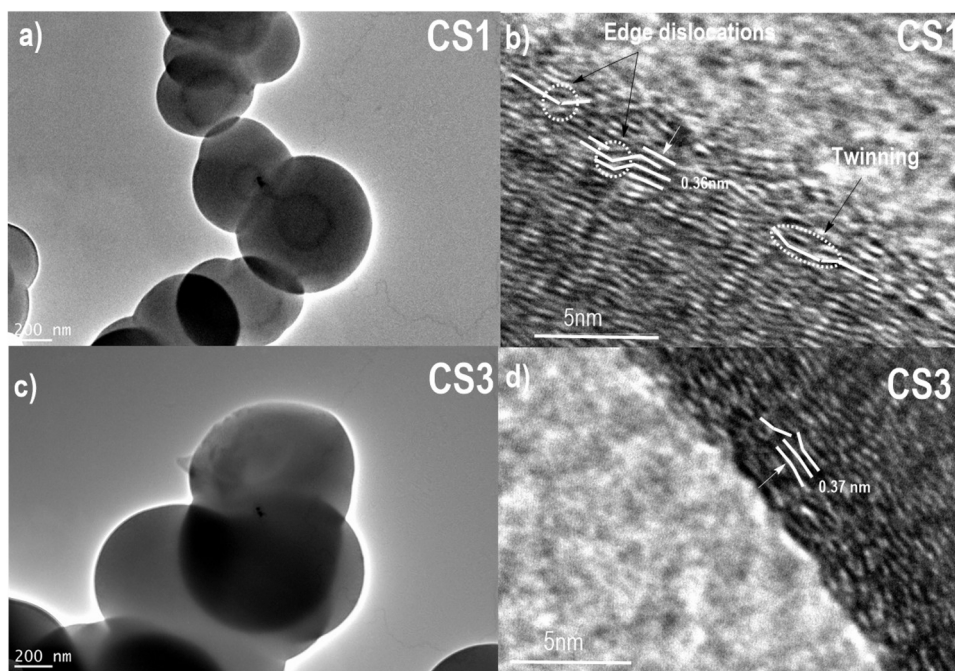


Fig. 3. TEM images of a. CS1 and c. CS3 samples at different magnifications. b) and d) images of spherical carbon near the edge (images b and d). The white lines indicated the structural modes of graphitic flakes. Only carbon spheres with the smallest (CS1) and largest (CS3) d_{002} spacing are shown in TEM images.

(TEM) measurements and only results obtained for CS1 (minimal interlayer spacing) and CS3 (maximal interlayer spacing) are shown in Fig. 3.

The single carbon sphere images are not regular, and the inner layers from the sphere center to the exterior surface are composed of graphitic flakes. As shown in Fig. 3a, particulates' agglomeration occurs in CS1.

The randomly grown graphitic flakes are visible at the gas and solid interface (Fig. 3b, d). The smallest size, short-range ordered structures of graphitic flakes are apparent in CS3, which is markedly influenced by the C_2H_2 concentration.

The deposition of graphite flakes in the vicinity of carbon sphere edges shows variations in surface roughness. We also calculated the

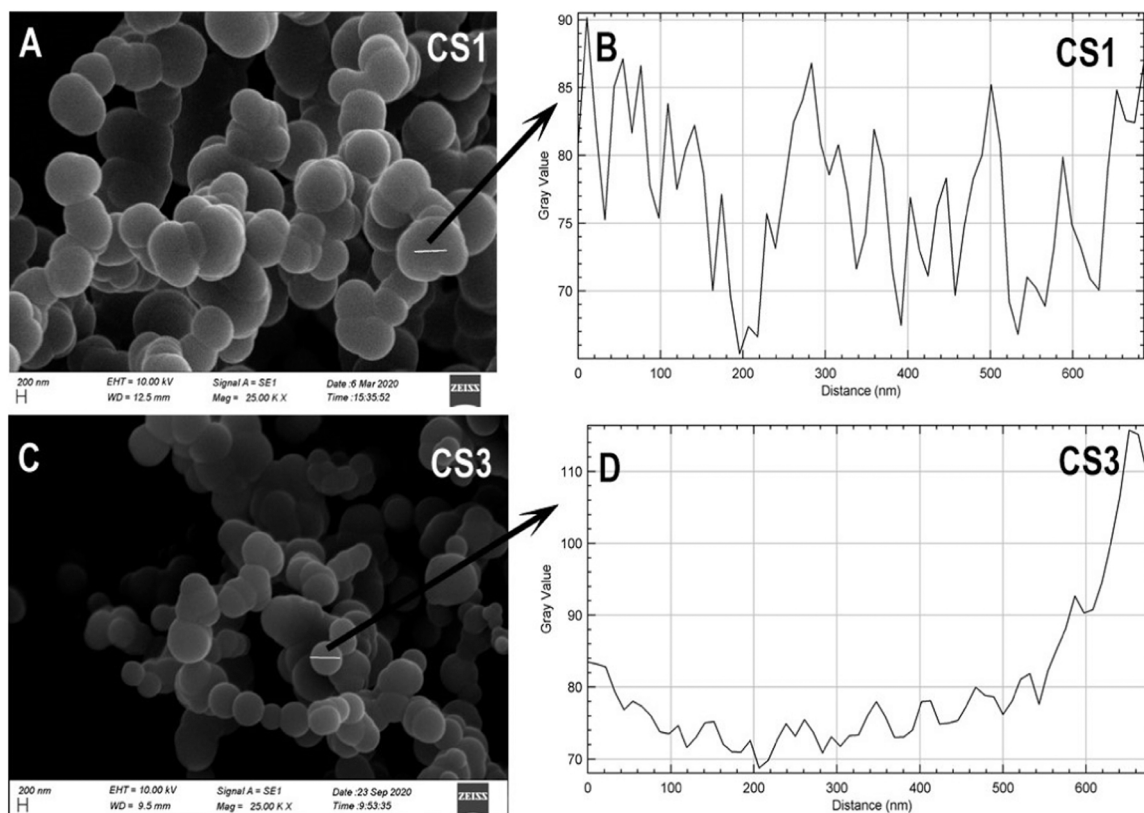


Fig. 4. Variation of the surface roughness (Gray Value in y-scale) laterally across on Sphere surface CS1, A. CS3, C. Gray Value plot of CS1, B. CS3, D.

degree of surface roughness using ImageJ software [71]. The Gray value resulting from the calculations indicates the degree of roughness [40]. Rapid fluctuations of the gray value mean the high roughness of the carbon spheres, and the data show that CS1 has a higher ruggedness than CS3 (Fig. 4B-D).

3.3. Carbon sphere formation via C pentagon structure

Based on the results presented, the postulated mechanistic steps for the carbon sphere formation are in agreement with vibration spectral data (Figs. 5 and 6). Around 1273 K, the C_2H_2 pyrolysis into PAH via benzene is well-known [53,72,73]. The exact ring configuration of the PAH depends on the system temperature and the C_2H_2 dosage used [53, 73]. At high C_2H_2 flows, PAH may nucleate, forming carbon spheres, and its dimension increases due to sporadic depositions of large PAH [53]. When the reactor temperature is varied between 500 and 2500 K, naphthalene is always formed by HACA mechanism [72,74–76]. Therefore at 1273 K and ambient atmospheric pressure, we assumed that the carbon sphere formation occurs via the naphthalene route [45] (Fig. 5). Accordingly, C_2H_2 converts into graphitic lattice structure via benzene naphthalene conversion route [53,75,76]. The Raman

vibrations shown at 1590 cm^{-1} represent the remanence of hexagonal carbon rings, and the one at 1355 cm^{-1} represents a disordered hexagonal carbon network (Fig. 3S) [77]. The IR bands at 1357 cm^{-1} and 1587 cm^{-1} represent the breathing vibrations of the hexagonal rings (Fig. 5 & 6). Thus, the formation of seven or five-membered C rings is feasible via in-plane rotation of the C–C bond in the hexagonal carbon ring by the Stone-Wales transformation route [78]. The three graphitic carbon rings (pentagonal, hexagonal, or heptagonal) consider in forming carbon spheres [61]. The hexagonal carbon network is the most stable of the three carbon ring structures.

Therefore, the stability and energetics of the other ring structures, e.g., pentagon and heptagons, were determined by molecular dynamics calculations (Fig. 1S). Here no surface defects or other microstructures were considered in the optimization. As shown in Table 1-S, compared to heptagon carbon rings, e.g., -150.805 eV per structure, the pentagon structure shows a lower total energy value, e.g., -167.530 eV per structure (Fig. 1-S and Table 1-S); hence, the carbon sphere formation is proposed via a pentagon route as shown in Fig. 5. Accordingly, the Fjord region of PAHs closes up into a pentagon ring structure by removing the hydrogen atoms according to acetylene addition to the edge via the HACA mechanism [79]. The characteristic IR bands at 635 cm^{-1} &

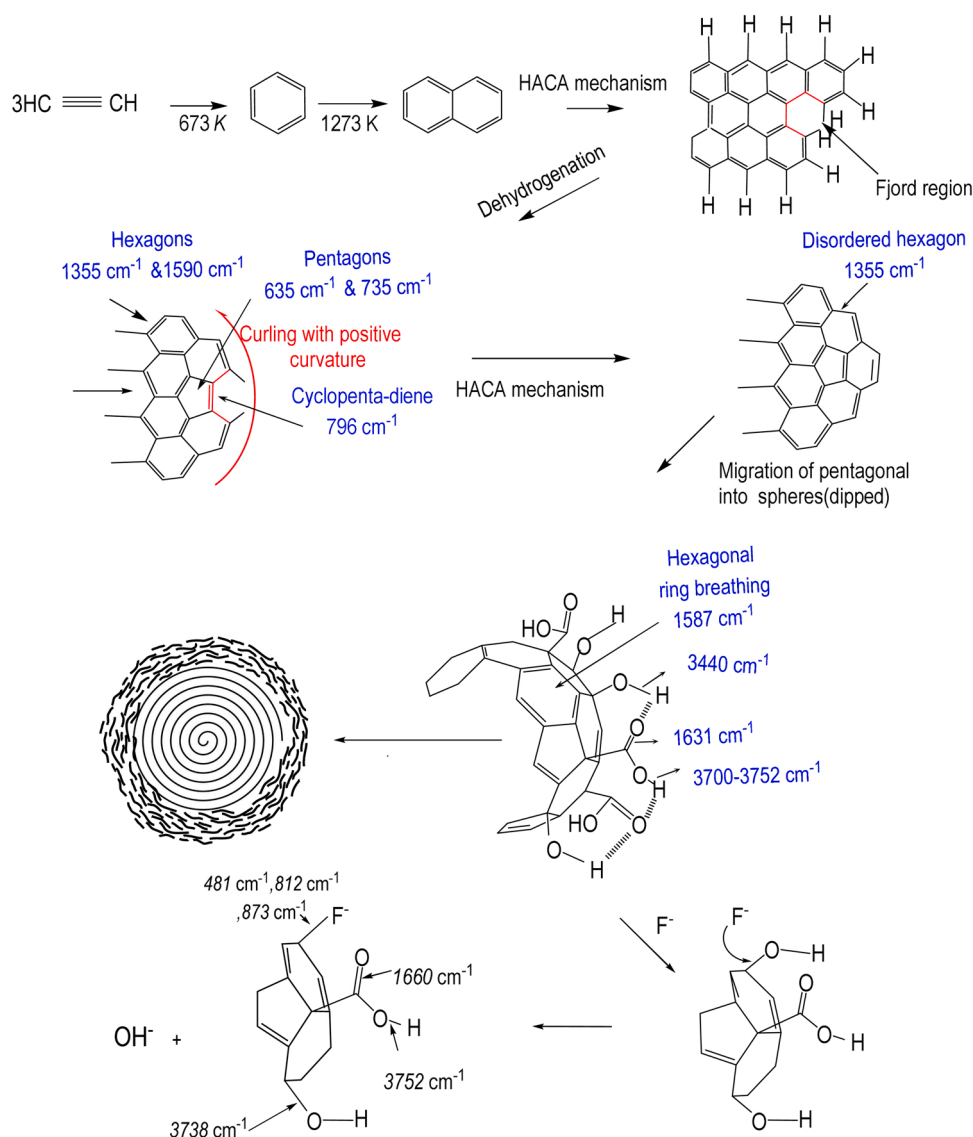


Fig. 5. The postulated mechanism for the pentagonal formation of carbon spheres - (dipped) from $C_2H_2 + C_6H_6$ reaction under CVD. Refer to Fig. 6 for the details of IR spectrums of bare (Fig. 3S, Raman spectrum) and fluoride adsorbed-CS3 (CS3-F).

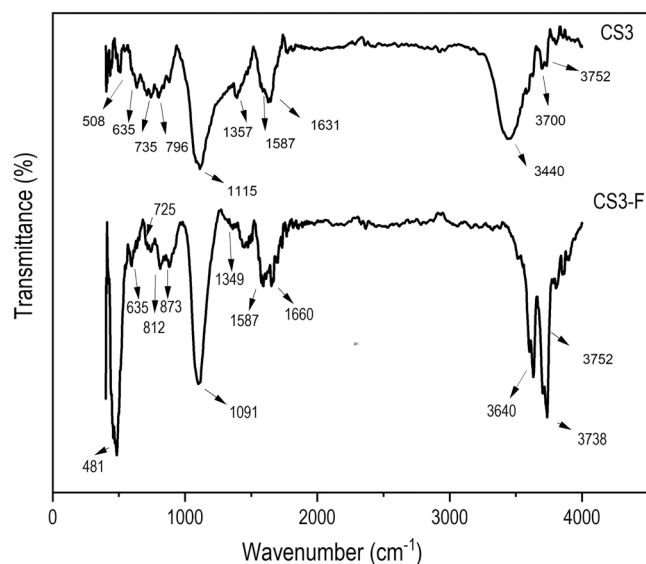


Fig. 6. FTIR spectra of CS3 and fluoride-adsorbed CS3 (CS3-F). The CS3 fluoride adsorption capacity is 14.8 mg/g.

796 cm^{-1} confirm the presence of pentagon carbon rings that facilitate curved surfaces. The IR band at 796 cm^{-1} evidence the formation of cyclopentadiene units in the structure (Fig. 6). Although inconclusive, the pentagonal carbon sphere is believed to be the dominant structure grown through the quasi-icosahedral shape [80].

3.4. Carbon sphere growth

Five processes believe to occur in carbon sphere growth: A. curved surface, B. nucleation, C. surface deposition, D. densification, and E. coalescence [28]. Accordingly, the pentagon carbon spheres (Fig. 7A) undergo spiral shell growth (B), and cyclic carbon rings are deposited on the carbon sphere surface, forming curved graphitic flakes (Fig. 7B). Thus, coalescence leads to nanospheres in high-temperature regions to minimize their potential energy [81](Fig. 7C). Variation of the dimension of the graphitic flakes results in tunable curvatures in compliance with the geometry of inner layers [61]. The carbon sphere binds readily with solid substrates, and also, they do agglomerate forming graphitic flakes (Fig. 7D). However, the re-deposition of graphitic flakes depends on substrate roughness and surface hydrophilicity (Fig. 7E) [51]. The carbon sphere formation mechanism depends on the experimental parameters such as the deposited surface and the nature of the surface sites vital for carbon nucleation [82].

3.5. X-ray photon spectroscopy of CS3 and CS3-fluoride species

High-resolution XPS measurements were carried out to probe the chemical state of C and O on the CS3 surface (Fig. 8a & b). Although the carbon sphere fabrication was carried out under inert conditions, the adventitious presence of oxygen on the solid surface is inevitable. The defects on the carbon sphere's surface, such as vacancies, curvature, and edge planes, are typical for oxygen adsorptive dissociation via HOMO (carbon sphere) to $2\pi^*$ (O_2) electron transfer [83]. $\left(\frac{I_D}{I_G}\right)$ Raman bands' intensity ratio dictates the surface's defects' nature CS3 has an intensity ratio of less than one (e.g., 0.91), which indicates the ubiquity of defects on the surface (Fig. 3S). In the presence of adventitious O_2 the graphitic carbon sphere was functionalized, yielding hydrophilic groups as -C-OH, -C=O, and -COOH [32,50]. Upon functionalization with O_2 , the $\left(\frac{O}{C}\right)$ ratio of carbon sphere was increased by about 10 times compared to the fresh carbon spheres, reducing the surface graphitic carbon [50].

The survey spectrum of CS3 and CS3-F is shown in Fig. 8a and b. The C1s segment of XPS spectra of CS3 and CS3-F can be deconvoluted into three peaks (Fig. 8e): the main peak observed around 284.8 eV shows the presence of C-C groups, while the other two peaks, around 285.8 eV and 286.4 eV occur due to the C-O and -COO-groups, respectively. Similarly, the three peaks are observed in the O 1s spectrum, and they are assigned to the C-O (532.5 eV), -COO (533.7 eV), and COOH groups (535.3 eV), respectively. Upon the adsorption of fluoride on CS3, the peaks correspond to C-O (shift $532.5 \rightarrow 532.6\text{ eV}$) and COOH (shift $535.3 \rightarrow 535.9\text{ eV}$) shifted positively, and a new peak appeared at 533.4 eV freeing of networked functional groups by none-bonded interactions (viz., coulombic and H bonding). The relative area of the -C-OH peak is over 50%, which shows the abundance of surface hydroxyl sites on CS3. After interacting CS3 with fluoride the relative areas of C-OH peak reduced ($69\% \rightarrow 65\%$) and O-C=O peak increased ($25\% \rightarrow 29\%$). However, the relative area of COOH peak (535.9 eV) shows no measurable difference (Fig. 8d). It implies that fluoride is adsorbed on CS3 mainly through anion exchange process at surface hydroxyl sites. Presence of low intensity peak at 291.08 eV corresponds to surface hydroxyl and fluoride interactions which further corroborate our arguments (Fig. 8f Inset). Accordingly, the non-specific fluoride adsorption on CS3 occurs via $\text{OH}^- \rightleftharpoons \text{F}^-$ anion exchange process, and further evidence is observed from IR data as shown in Fig. 6. The IR bands at 1631 cm^{-1} and 3440 cm^{-1} confirm stretching vibrations in the C=O, and O-H, respectively. The IR bands at 481 cm^{-1} (out-of-plane vibrations), 812 cm^{-1} (in-plane vibrations), and 873 cm^{-1} (diffraction) are distinct on CS3-F samples [84]. In addition, the broad band around 3400 cm^{-1} , corresponding to the -OH stretch converted into discrete bands at 3640, 3752, and 3738 cm^{-1} upon F- addition as a result of freeing a H-bonded network of CS3 (Fig. 5). Both experimental observations are in agreement and point to an anion exchange mechanism for

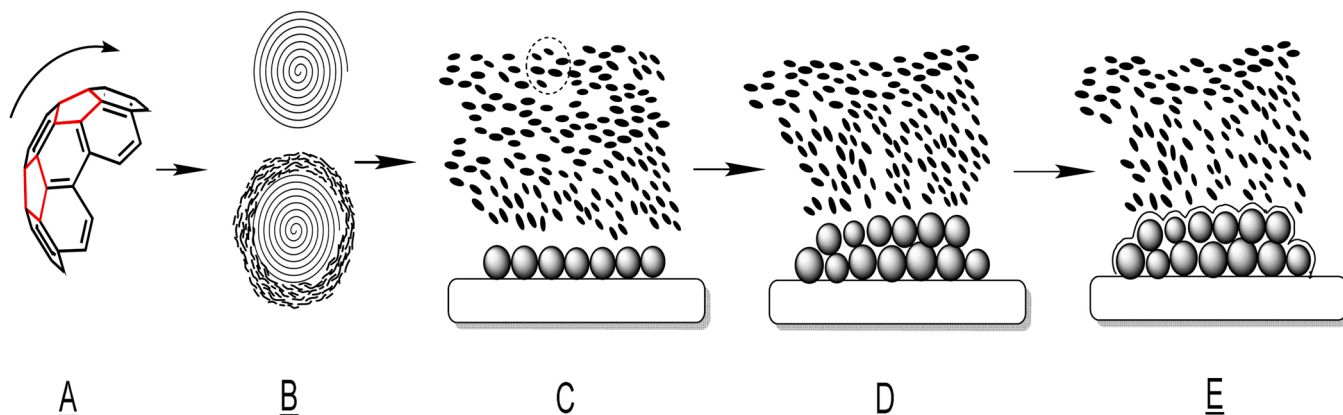


Fig. 7. Growth process of carbon sphere. A. pentagon curved surface, B. homogeneous nucleation, C. particle deposition, D. densification, and E. coalescence.

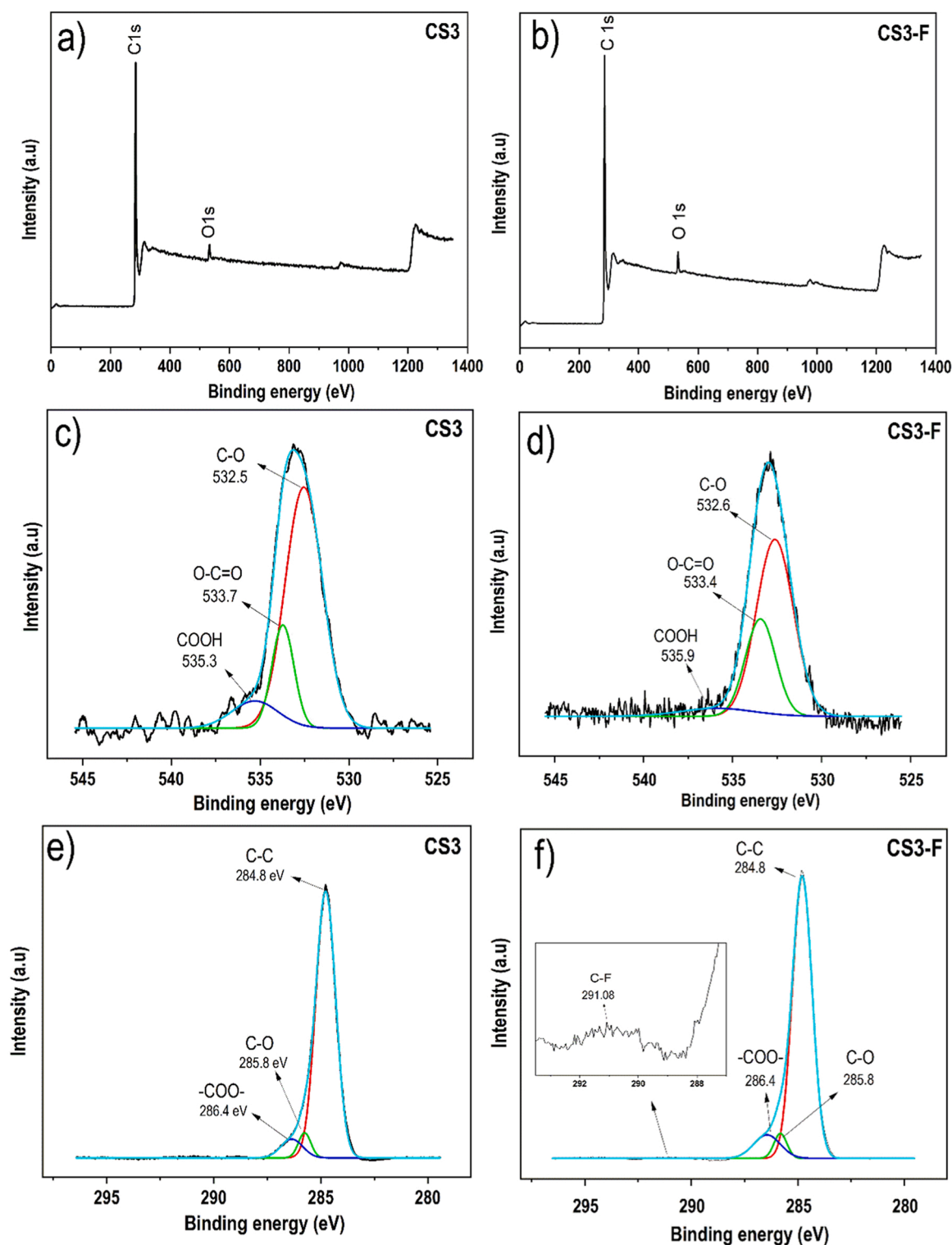


Fig. 8. XPS spectra (a) survey graph of CS3 (b) survey graph of CS3-F, (c) O 1s spectra of CS3 (d) O 1s spectra of CS3-F (e) C 1s spectra of CS3 and (f) C 1s spectra of CS3-F.

fluoride adsorption by CS3.

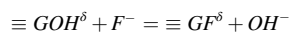
3.6. Carbon sphere for water defluoridation

The surface sites of carbon spheres hydroxylate in contact with the water (Fig. 4S). The exact nature of these surface sites is not resolved yet; however, they are believed to occur via H-bonded water dissociation at the polar C-derived defect zones [85]. In any case, creating surface

hydroxyl sites is vital (designated as $\equiv GOH^\delta$, where δ represents a partial charge on C based on Pauling bond valence calculations, e.g., -0.10 to -0.50 partial charge) for solutes retention on carbon spheres [86]. As shown in proton titration data (Fig. 4S), the pH_{zpc} of carbon spheres is around 8.29 showing a positive surface when the solution pH ranges between 5.60 and 7.00, e.g., a typical pH of the most natural water bodies.

The highest fluoride adsorption by carbon spheres is shown for CS3

(details in Fig. 5S). The solution pH has increased upon fluoride addition releasing OH^- from the CS3 surface. Within the limit of experimental uncertainty, the OH^-/F^- exchange ratio converges to 0.93 dominating an anion exchange process for the fluoride removal by CS3 as shown below.



The zeta potential values of bare and fluoride-treated CS3 values do not change appreciably signifying the anion exchange process for fluo-

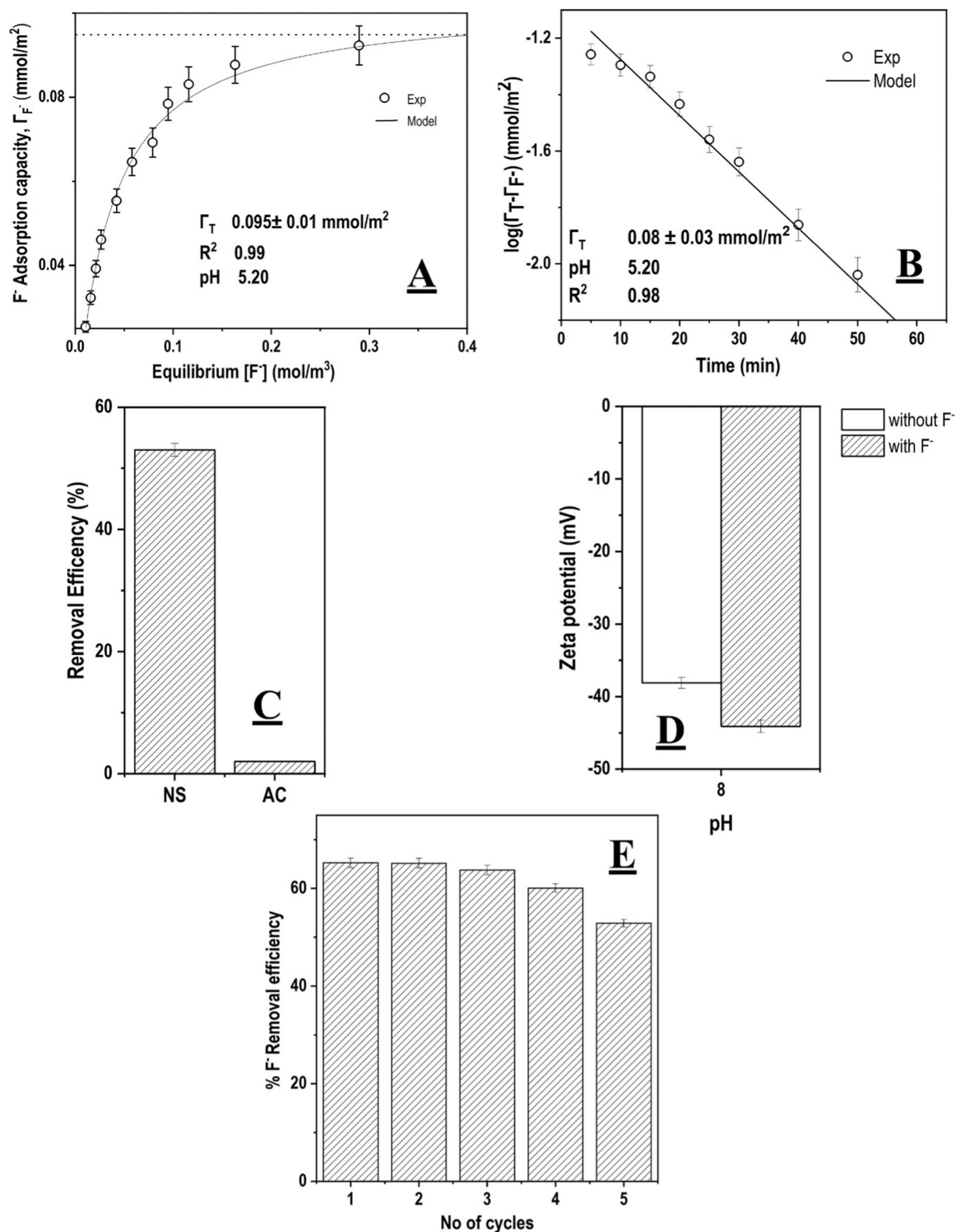


Fig. 9. (A - E): A: Fluoride adsorption isotherm on CS3. Initial F⁻ concentration 0.039–0.526 mM, pH ~5.20, 0.01 M NaCl, T 298 K). B: Fluoride adsorption kinetics on CS3. Initial [F⁻] = 0.105 ± 0.01 mM, pH 5.2, 0.01 NaCl, T 298 K. $\log(\Gamma_e - \Gamma_t) = \log(\Gamma_e) - \frac{k_1 t}{2.303}$ where Γ_e and Γ_t are fluoride adsorption density at equilibrium and any time and k_1 represents pseudo first order rate constant. C. The groundwater fluoride removal efficiency by CS3. A natural water sample was spiked with 0.105 mM [F⁻]. Chemical composition of groundwater before spiking: pH 7.20, TDS 669 mg/L, total hardness 396 mg/L, CaCO_3 , F 1 mg/L (0.053 mM). AC represents activated carbon [87]. D. variation of zeta potential of CS3 and CS3 - F particulates. Error bars $\pm 2\%$ E: Fluoride removal efficiency on repeated use of CS3. Initial [F⁻] 0.121 ± 0.001 mM, pH 5.20 ± 0.01 , regenerant 0.10 M NaOH.

ride removal (Fig. 9. D). As shown in Fig. 9B, when initial $\left(\frac{=GOH}{F^-}\right) > 1$, the chemical kinetics of fluoride adsorption by CS3 follows pseudo-first-order law. Maximum fluoride adsorption capacity by CS3 is observed around pH 5–7. At this pH range, the fluoride adsorption by CSx (x = 1–5) with different sizes was also determined (Fig. 9A). The CS3 shows the highest fluoride adsorption due to the high surface area-to-volume ratio. The effect of CS curvature on the fluoride adsorption process is not yet clear [88]. However, the abundance of surface defects increased favorable sites for fluoride adsorption [22]. The activated carbon shows minute proportions of fluoride adsorption (Fig. 9C). As shown in earlier sections, the carbon sphere surface seems to be heterogeneous. Here, the BET surface area of CS3 is 7.603 m²/g, which is slightly higher than that of pristine CS [48]. This result indicates smoother surface morphology of CS3 than CS1. The mean pore diameter was 4.2 nm and a very low total pore volume of 0.008 cc/g CS was measured for CS3 due to the low porosity of solid spheres. However, fluoride adsorption on CS3 follows the Langmuir model with 0.08 mmol/m² surface coverage (Fig. 9B). The Langmuir model assumes homogeneous surface sites at a given pH and solutes concentration. The heterogeneous carbon sphere surface is believed to consist of a large array of islands with homogeneity. At a given fluoride loading, such a homogeneous island becomes activated, which results in F⁻ adsorption on CS3 following the Langmuir model. The fluoride removal efficiency of CS3 was also examined using a groundwater sample from Sri Lanka with the following composition: pH 7.20, TDS 669 mg/L, total hardness 396 mg/L, CaCO₃, F 1 mg/L. As shown in Fig. 9C, over 50% of fluoride is removed by CS3. The high solute levels in groundwater exert reduced fluoride removal efficiency. As shown in Figure 10. E, the fluoride removal efficiency was also examined after repeated use of the substrate (CS3) for five times. Herein the spent CS3 was regenerated with 0.01 M NaOH at the end of each cycle. The fluoride removal efficiency of CS3 is not diminished after cyclic use showing almost perfect reversibility of the surface sites for ion exchange processes.

4. Conclusions

We successfully fabricated size-tunable carbon spheres by chemical vapor deposition using C₂H₂ and N₂ gas precursors. The diameter of the carbon spheres varies with the precursor gas flow ratio yielding a minimal size at $\left(\frac{C_2H_2}{N_2}\right) = \frac{5}{6}$ (viz. CS3). Molecular spectroscopic data suggest the ubiquity of defects on the surface of carbon spheres. Upon contact with the water, the carbon spheres readily hydroxylate showing positively charged surface sites ($=GOH^{\delta}$) when pH falls within ~5.00 to ~7.00, e.g., typical of natural water pH. Zeta potential measurements can be used to elucidate anion exchange mechanism for fluoride retention on the CS hydroxylated sites, viz. $=GOH^{\delta}$. The carbon sphere shows a promise in de-contaminating fluoride-rich groundwaters. The inconclusive evidence for the formation of CS via carbon pentagons is shown presently. Using NEXAFS measurements, Further research is underway using NEXAFS measurements, to probe pentagon defects precisely in hexagonal graphitic structures to confirm the CS formation mechanism shown in this work.

CRediT authorship contribution statement

B.V.N. Sewwandi: Data curation, Formal analysis, Investigation, Writing – original draft. **P. M. C. J. Bandara:** Methodology, reviewing, and editing. **L. Jayaratna:** Methodology, reviewing, and editing. **Himal Wijekoon:** Methodology, reviewing, and editing (MD calculations). **Z. Wu:** Methodology, Resources. **A.R. Kumarasinghe:** Supervision, reviewing, and editing. **Athula Bandara:** Conceptualization, Validation (spectroscopy). **Rohan Weerasooriya:** Project administration, Investigation, Funding acquisition, reviewing, Supervision, Validation, reviewing, and editing. **Xing Chen:** Project administration,

Investigation, Funding acquisition, reviewing, Supervision, Validation, reviewing, and editing.

Declaration of Competing Interest

The authors declare that they have no known competing financial interests or personal relationships that could have appeared to influence the work reported in this paper.

Data Availability

Data will be made available on request.

Acknowledgments

This research work was supported by the National Research Council of Sri Lanka under a target-driven grant (NRC-TO-16–015). Reviewer comments enhanced manuscript quality.

Appendix A. Supporting information

Supplementary data associated with this article can be found in the online version at doi:10.1016/j.colsurfa.2023.131582.

References

- [1] T.L. Tan, P.A. Krunamurthy, H. Nakajima, S.A. Rashid, Adsorptive, kinetics and regeneration studies of fluoride removal from water using zirconium-based metal organic frameworks, RSC Adv. 10 (32) (2020) 18740–18752, <https://doi.org/10.1039/d0ra01268h>.
- [2] P.J. Mullenix, A new perspective on metals and other contaminants in fluoridation chemicals, Int J. Occup. Environ. Health 20 (2) (2014) 157–166, <https://doi.org/10.1179/2049396714Y.0000000062>.
- [3] RS2. Guidelines for Drinking-water Quality.; 2017.
- [4] L.F. He, J.G. Chen, DNA damage, apoptosis and cell cycle changes induced by fluoride in rat oral mucosal cells and hepatocytes, World J. Gastroenterol. 12 (7) (2006) 1144–1148, <https://doi.org/10.3748/wjg.v12.i7.1144>.
- [5] X.Z. Xiong, J.L. Liu, W.H. He, et al., Dose-effect relationship between drinking water fluoride levels and damage to liver and kidney functions in children, Environ. Res 103 (1) (2007) 112–116, <https://doi.org/10.1016/j.envres.2006.05.008>.
- [6] E.T. Everett, Critical reviews in oral biology & medicine: Fluoride's effects on the formation of teeth and bones, and the influence of genetics, J. Dent. Res 90 (5) (2011) 552–560, <https://doi.org/10.1177/0022034510384626>.
- [7] H. Akbari, D. Balarak, M. Yousefi, P. Rigi, A.H. Mahvi, Fluoride removal from aqueous solution by almond shell Activated carbon, Publ. Online (2021) 269–283.
- [8] S. Waghmare, S. Arfin, T. Fluoride removal from water by adsorption-a review, Int. J. Innov. Sci. Eng. Technol. 2 (9) (2015), <https://doi.org/10.1016/j.cej.2011.05.028>.
- [9] A.H. Mahvi, F.K. Mostafapour, D. Balarak, A.D. Khatibi, Adsorption of fluoride from aqueous solutions by a chitosan/zeolite composite, Fluoride 52 (October) (2019) 546–552.
- [10] El-Salam M.H.A. Applications of Reverse Osmosis. Encycl Food Sci Nutr (Second Ed. 2003;(1997):3833–3837.
- [11] R. Das, Advanced membrane materials for desalination: carbon nanotube and graphene, Publ. Online (2017) 322–342, <https://doi.org/10.21741/9781945291357-10>.
- [12] G.P.S. Ibrahim, A.M. Isloor, E. Yuliwati, A.F. Ismail, Carbon-Based Nanocomposite Membranes for Water and Wastewater Purification, Elsevier Inc, 2018, <https://doi.org/10.1016/B978-0-12-814503-6.00002-1>.
- [13] M.J. Eckelman, M.S. Mauter, J.A. Isaacs, M. Elimelech, New perspectives on nanomaterial aquatic ecotoxicity: Production impacts exceed direct exposure impacts for carbon nanotubes, Environ. Sci. Technol. 46 (5) (2012) 2902–2910, <https://doi.org/10.1021/es203409a>.
- [14] L. Chen, C. Wang, S. Yang, et al., Chemical reduction of graphene enhances in vivo translocation and photosynthetic inhibition in pea plants, Environ. Sci. Nano 6 (4) (2019) 1077–1088, <https://doi.org/10.1039/c8en01426d>.
- [15] W. Hirunpinyopas, P. Iamprasertkun, M.A. Bissett, R.A.W. Dryfe, Tunable charge/size selective ion sieving with ultrahigh water permeance through laminar graphene membranes, Carbon N. Y 156 (2020) 119–129, <https://doi.org/10.1016/j.carbon.2019.09.030>.
- [16] J. Xu, Z. Cao, Y. Zhang, et al., A review of functionalized carbon nanotubes and graphene for heavy metal adsorption from water: Preparation, application, and mechanism, Chemosphere 195 (2018) 351–364, <https://doi.org/10.1016/j.chemosphere.2017.12.061>.
- [17] R. Das, B.F. Leo, F. Murphy, The toxic truth about carbon nanotubes in water purification: a perspective view, Nanoscale Res Lett. (2018) 13, <https://doi.org/10.1186/s11671-018-2589-z>.

- [18] Z. Yang, Z. Li, M. Xu, et al., Controllable synthesis of fluorescent carbon dots and their detection application as nanoprobe, *Micro Nano Lett.* 5 (4) (2013) 247–259.
- [19] Yang S. tao, Wang X., Wang H., et al. Carbon Dots as Nontoxic and High-Performance Fluorescence Imaging Agents. Published online 2009:18110–18114.
- [20] J. Wang, Z. Hu, J. Xu, Y. Zhao, Therapeutic applications of low-toxicity spherical nanocarbon materials, *NPG Asia Mater.* (11) (2014), <https://doi.org/10.1038/am.2013.79>.
- [21] J. Rivera-Utrilla, M. Sánchez-Polo, V. Gómez-Serrano, P.M. Álvarez, M.C.M. Alvim-Ferraz, J.M. Dias, Activated carbon modifications to enhance its water treatment applications. An overview, *J. Hazard Mater.* 187 (1–3) (2011) 1–23, <https://doi.org/10.1016/j.jhazmat.2011.01.033>.
- [22] Z.C. Kang, Z.L. Wang, Chemical activities of graphitic carbon spheres, *J. Mol. Catal. A Chem.* 169 (96) (1997) 215–222, [https://doi.org/10.1016/S1381-1169\(96\)00393-7](https://doi.org/10.1016/S1381-1169(96)00393-7).
- [23] M. Manoukian, H. Tavakol, H. Fashandi, Synthesis of Highly Uniform Sulfur-Doped Carbon Sphere Using CVD Method and Its Application for Cationic Dye Removal in Comparison with Undoped Product, Elsevier B.V., 2018, <https://doi.org/10.1016/j.jce.2018.10.026>.
- [24] M. Li, C. Wang, M.J.O. Connell, C.K. Chan, Carbon nanosphere adsorbents for removal of arsenate and selenate from water, *Environ. Sci. Nano.* (2015), <https://doi.org/10.1039/C4EN00204K>.
- [25] G. Patiño-guillén, A. Arceta-lozano, J.A. Falcón-montes, et al., Simple in situ functionalization of carbon nanospheres, *Publ. Online* (2021), <https://doi.org/10.1088/1361-6528/abc8b3>.
- [26] X. Song, P. Gunawan, R. Jiang, S.S.J. Leong, K. Wang, R. Xu, Surface activated carbon nanospheres for fast adsorption of silver ions from aqueous solutions, *J. Hazard Mater.* 194 (August) (2011) 162–168, <https://doi.org/10.1016/j.jhazmat.2011.07.076>.
- [27] K.L.A. Cao, F. Iskandar, E. Tanabe, T. Ogi, Recent advances in the fabrication and functionalization of nanostructured carbon spheres for energy storage applications, *KONA Powder Part J.* 2023 (40) (2023) 197–218, <https://doi.org/10.14356/kona.2023016>.
- [28] C.M. Lei, W.L. Yuan, H.C. Huang, S.W. Ho, C.J. Su, Synthesis and conductivity measurement of carbon spheres by catalytic CVD using non-magnetic metal complexes, *Synth. Met* 161 (15–16) (2011) 1590–1595, <https://doi.org/10.1016/j.synthmet.2011.05.023>.
- [29] B.K. Mutuma, R. Rodrigues, K. Ranganathan, B. Matsoso, D. Wamwangi, N. J. Coville, Hollow carbon spheres and a hollow carbon sphere / polyvinylpyrrolidone composite as ammonia sensors, *J. Mater. Chem. A* 5 (2016) 2539–2549, <https://doi.org/10.1039/C6TA09424D>.
- [30] L. Zhang, M. Yao, W. Yan, et al., Delivery of a chemotherapeutic drug using novel hollow carbon spheres for esophageal cancer treatment, *Int. J. Nanomed.* 12 (2017) 6759–6769, <https://doi.org/10.2147/IJN.S142916>.
- [31] H. Zhang, X. li Zhou, L. ming Shao, F. Lu, P. jing He, Hierarchical porous carbon spheres from low-density polyethylene for high-performance supercapacitors, *ACS Sustain Chem. Eng.* 7 (2019) 3801–3810, <https://doi.org/10.1021/acssuschemeng.8b04539>.
- [32] A.A. Deshmukh, S.D. Mhlanga, N.J. Coville, Carbon spheres, *Mater. Sci. Eng. R. Rep.* 70 (1–2) (2010) 1–28, <https://doi.org/10.1016/j.mser.2010.06.017>.
- [33] Z.C. Kang, Z.L. Wang, On accretion of nanosize carbon spheres, *J. Phys. Chem.* 100 (13) (1996) 5163–5165, <https://doi.org/10.1021/jp9535809>.
- [34] V.G. Pol, S.V. Pol, J.M. Calderon Moreno, A. Gedanken, High yield one-step synthesis of carbon spheres produced by dissociating individual hydrocarbons at their autogenic pressure at low temperatures, *Carbon N. Y* 44 (15) (2006) 3285–3292, <https://doi.org/10.1016/j.carbon.2006.06.023>.
- [35] V.G. Pol, M. Motiei, A. Gedanken, J. Calderon-Moreno, M. Yoshimura, Carbon spheres: Synthesis, properties and mechanistic elucidation, *Carbon N. Y* 42 (1) (2004) 111–116, <https://doi.org/10.1016/j.carbon.2003.10.005>.
- [36] R. Purohit, K. Purohit, S. Rana, R.S. Rana, V. Patel, Carbon nanotubes and their growth methods, *Procedia Mater. Sci.* 6 (Icmpec) (2014) 716–728, <https://doi.org/10.1016/j.mspro.2014.07.088>.
- [37] S. Feshki, M. Marandi, Synthesis of carbon spheres of controlled size by hydrothermal method, *J. Nanostruct.* 4 (3) (2014) 295–301. (https://jns.kashanu.ac.ir/article_7995.html).
- [38] J.Y. Miao, D.W. Hwang, K.V. Narasimhulu, et al., Synthesis and properties of carbon nanospheres grown by CVD using Kaolin supported transition metal catalysts, *Carbon N. Y* 42 (4) (2004) 813–822, <https://doi.org/10.1016/j.carbon.2004.01.053>.
- [39] N. Hasheminejad, H. Tavakol, W. Salvenmoser, Preparation of gold-decorated simple and sulfur-doped carbon spheres for desulfurization of fuel, *J. Clean. Prod.* 264 (2020), 121684, <https://doi.org/10.1016/j.jclepro.2020.121684>.
- [40] B.V.N. Sewwandi, A.R. Kumarasinghe, D. Tushara, et al., Fabrication of size-tunable graphitized carbon spheres with hierarchical surface morphology on p-Si (100) by chemical vapour deposition, *Sri Lankan J. Phys.* 22 (1) (2021) 80, <https://doi.org/10.4038/sljp.v22i1.8093>.
- [41] P. Bakhshi, H. Tavakol, Oil removal from water using highly hydrophobic, ultralight carbon microspheres, *Int. J. Environ. Sci. Technol.* (0123456789) (2019), <https://doi.org/10.1007/s13762-019-02495-0>.
- [42] H.S. Qian, F.M. Han, B. Zhang, Y.C. Guo, J. Yue, B.X. Peng, Non-catalytic CVD preparation of carbon spheres with a specific size, *Carbon N. Y* 42 (4) (2004) 761–766, <https://doi.org/10.1016/j.carbon.2004.01.004>.
- [43] Y. Zhang, W. Yang, R.Y. Luo, H.D. Shang, Preparation of carbon nanospheres by non-catalytic chemical vapor deposition and their formation mechanism, *Xinjing Tan. Cailiao/N. Carbon Mater.* 31 (5) (2016) 467–474, [https://doi.org/10.1016/S1872-5805\(16\)60025-2](https://doi.org/10.1016/S1872-5805(16)60025-2).
- [44] A.D. Faisal, A. Aljubouri, Synthesis and production of carbon nanospheres using noncatalytic CVD method, *Int. J. Adv. Mater. Res* 2 (5) (2016) 86–91.
- [45] M. Inagaki, Room temperature exfoliation of graphite micrographite, *Carbon N. Y* 31 (4) (1993) 1349–1350, [https://doi.org/10.1016/0008-6223\(93\)90096-S](https://doi.org/10.1016/0008-6223(93)90096-S).
- [46] Z. Ereš, S. Hrabar, Low-cost synthesis of high-quality graphene in do-it-yourself CVD reactor, *Automatika* 59 (3) (2018) 255–261, <https://doi.org/10.1080/00051144.2018.1528691>.
- [47] B. Chang, D. Guan, Y. Tian, Z. Yang, X. Dong, Convenient synthesis of porous carbon nanospheres with tunable pore structure and excellent adsorption capacity, *J. Hazard Mater.* 262 (2013) 256–264, <https://doi.org/10.1016/j.jhazmat.2013.08.054>.
- [48] R. Panicker, C.B. Sobhan, S. Chakravorti, Chemical vapor deposition synthesis of carbon spheres: effects of temperature and hydrogen, *Vacuum* 172 (November 2019) (2020), 109108, <https://doi.org/10.1016/j.vacuum.2019.109108>.
- [49] C. Leishan, Controlled synthesis of carbon spheres using iron catalyst supported on aluminum hydroxide, *Adv. Mater.* Res 641–642 (1) (2013) 47–50, <https://doi.org/10.4028/www.scientific.net/AMR.641-642.47>.
- [50] H.C. Wu, C.T. Hong, H.T. Chiu, Y.Y. Li, Continuous synthesis of carbon spheres by a non-catalyst vertical chemical vapor deposition, *Diam. Relat. Mater.* 18 (4) (2009) 601–605, <https://doi.org/10.1016/j.diamond.2008.10.047>.
- [51] Z.X. Xu, J.D. Lin, V.A.L. Roy, Y. Ou, D.W. Liao, Catalytic synthesis of carbon nanotubes and carbon spheres using Kaolin supported catalyst, *Mater. Sci. Eng. B Solid-State Mater. Adv. Technol.* 123 (2) (2005) 102–106, <https://doi.org/10.1016/j.mseb.2005.07.012>.
- [52] T. Bensabath, H. Monnier, P.A. Glaude, Detailed kinetic modeling of the formation of toxic polycyclic aromatic hydrocarbons (PAHs) coming from pyrolysis in low-pressure gas carburizing conditions, *J. Anal. Appl. Pyrolysis* 122 (2016) 342–354, <https://doi.org/10.1016/j.jaap.2016.09.007>.
- [53] T. Bensabath, M.D. Le, H. Monnier, P.A. Glaude, Polycyclic aromatic hydrocarbon (PAH) formation during acetylene pyrolysis in tubular reactor under low pressure carburizing conditions, *Chem. Eng. Sci.* 202 (2019) 84–94, <https://doi.org/10.1016/j.ces.2019.03.030>.
- [54] C. Saggese, N.E. Sánchez, A. Frassoldati, et al., Kinetic modeling study of polycyclic aromatic hydrocarbons and soot formation in acetylene pyrolysis, *Energy Fuels* 28 (2) (2014) 1489–1501, <https://doi.org/10.1021/ef402048q>.
- [55] M.H. Back, Mechanism of the pyrolysis of acetylene, *Can. J. Chem.* 49 (13) (1971) 2199–2204, <https://doi.org/10.1139/v71-359>.
- [56] C.F. Cullis, N.H. Franklin, The pyrolysis of acetylene at temperatures from 500 to 1000 °C, *Proc. R. Soc. Lond. Ser. A Math. Phys. Sci.* 280 (1380) (1964) 139–152, <https://doi.org/10.1098/rspa.1964.0136>.
- [57] K. Norinaga, O. Deuschmann, K.J. Hüttinger, Analysis of gas phase compounds in chemical vapor deposition of carbon from light hydrocarbons, *Carbon N. Y* 44 (9) (2006) 1790–1800, <https://doi.org/10.1016/j.carbon.2005.12.050>.
- [58] B. Shukla, M. Koshi, A novel route for PAH growth in HACA based mechanisms, *Combust. Flame* 159 (12) (2012) 3589–3596, <https://doi.org/10.1016/j.combustflame.2012.08.007>.
- [59] N.E. Sánchez, A. Callejas, Á. Millera, R. Bilbao, M.U. Alzueta, Determination of polycyclic aromatic hydrocarbons (PAH) adsorbed on soot formed in pyrolysis of acetylene at different temperatures, *Chem. Eng. Trans.* 22 (2010) 131–136, <https://doi.org/10.3303/CET1022021>.
- [60] N.E. Sánchez, A. Callejas, Á. Millera, R. Bilbao, M.U. Alzueta, Polycyclic aromatic hydrocarbon (PAH) and soot formation in the pyrolysis of acetylene and ethylene: Effect of the reaction temperature, *Energy Fuels* 26 (8) (2012) 4823–4829, <https://doi.org/10.1021/ef300749q>.
- [61] Z.L. Wang, Z.C. Kang, Pairing of pentagonal and heptagonal carbon rings in the growth of nanosize carbon spheres synthesized by a mixed-valent oxide-catalytic carbonization, *Process* 3654 (001) (1996) 17725–17731.
- [62] A. Nieto-m, R. Romero, A. Romero, J.L. Valverde, Carbon nanospheres: synthesis, physicochemical properties and applications, *J. Mater. Chem. (Level 1)* (2011) 1664–1672, <https://doi.org/10.1039/c0jm01350a>.
- [63] N. Hasheminejad, H. Tavakol, W. Salvenmoser, Preparation of gold-decorated simple and sulfur-doped carbon spheres for desulfurization of fuel, *J. Clean. Prod.* 264 (2020), 121684, <https://doi.org/10.1016/j.jclepro.2020.121684>.
- [64] A.P. Thompson, H.M. Aktulga, R. Berger, et al., LAMMPS - a flexible simulation tool for particle-based materials modeling at the atomic, meso, and continuum scales, *Comput. Phys. Commun.* 271 (2022), 108171, <https://doi.org/10.1016/j.cpc.2021.108171>.
- [65] S.J. Stuart, A.B. Tutein, J.A. Harrison, A reactive potential for hydrocarbons with intermolecular interactions, *J. Chem. Phys.* 112 (14) (2000) 6472–6486, <https://doi.org/10.1063/1.481208>.
- [66] Handbook of Nanophase and Nanostructured Materials: Synthesis - Google Books. Accessed June 29, 2022. https://books.google.lk/books?redir_esc=y&id=q6_N9mTj38C&q=CVD#v=snippet&q=homogeneous&f=false.
- [67] L. Chen, C. Wang, Synthesis of carbon spheres with controllable size distribution by chemical vapor deposition, *Adv. Mater.* Res 490–495 (2012) 3807–3810, <https://doi.org/10.4028/www.scientific.net/AMR.490-495.3807>.
- [68] G.F. Malgas, C.J. Arendse, N.P. Cele, F.R. Cummings, Effect of mixture ratios and nitrogen carrier gas flow rates on the morphology of carbon nanotube structures grown by CVD, *J. Mater. Sci.* 43 (3) (2008) 1020–1025, <https://doi.org/10.1007/s10853-007-2230-5>.
- [69] K. Jurkiewicz, M. Pawlyta, A. Burian, Structure of carbon materials explored by local transmission electron microscopy and global powder diffraction probes, *J. Carbon Res* 4 (4) (2018) 68, <https://doi.org/10.3390/c4040068>.
- [70] F. Mori, M. Kubouchi, Y. Arao, Effect of graphite structures on the productivity and quality of few-layer graphene in liquid-phase exfoliation, *J. Mater. Sci.* 53 (18) (2018) 12807–12815, <https://doi.org/10.1007/s10853-018-2538-3>.

- [71] ImageJ. Accessed January 20, 2021. <https://imagej.net/Welcome>.
- [72] A.M. Mebel, Y. Georgievskii, A.W. Jasper, S.J. Klippenstein, Temperature- and pressure-dependent rate coefficients for the HACA pathways from benzene to naphthalene, *Proc. Combust. Inst.* 36 (1) (2017) 919–926, <https://doi.org/10.1016/j.proci.2016.07.013>.
- [73] N.E. Sánchez, A. Callejas, A. Millera, R. Bilbao, M.U. Alzueta, Formation of PAH and soot during acetylene pyrolysis at different gas residence times and reaction temperatures, *Energy* 43 (1) (2012) 30–36, <https://doi.org/10.1016/j.energy.2011.12.009>.
- [74] T.C. Chu, Z.J. Buras, M.C. Smith, A.B. Uwagwu, W.H. Green, From benzene to naphthalene: Direct measurement of reactions and intermediates of phenyl radicals and acetylene, *Phys. Chem. Chem. Phys.* 21 (40) (2019) 22248–22258, <https://doi.org/10.1039/c9cp04554f>.
- [75] V.V. Kislov, A.I. Sadovnikov, A.M. Mebel, Formation mechanism of polycyclic aromatic hydrocarbons beyond the second aromatic ring, *J. Phys. Chem. A* 117 (23) (2013) 4794–4816, <https://doi.org/10.1021/jp402481y>.
- [76] Kholghy M.R. The Evolution of Soot Morphology in Laminar Co-Flow Diffusion Flames of the Surrogates for Jet A-1 and a Synthetic Kerosene. 2012;(April):94.
- [77] K.N. Kudin, B. Ozbas, H.C. Schniepp, R.K. Prud, I.A. Aksay, R. Car, Raman spectra of graphite oxide and functionalized graphene sheets, *Nano Lett.* 8 (1) (2008) 36–41.
- [78] D. Campisi, A. Candian, Do defects in PAHs promote catalytic activity in space? Stone-Wales pyrene as a test case, *Phys. Chem. Chem. Phys.* 22 (12) (2020) 6738–6748, <https://doi.org/10.1039/c9cp06523g>.
- [79] C.J. Mackie, E. Peeters, C.W. Bauschlicher, J. Cami, Characterizing the infrared spectra of small, neutral, fully dehydrogenated polycyclic aromatic hydrocarbons, *Astrophys J.* 799 (2) (2015), <https://doi.org/10.1088/0004-637X/799/2/131>.
- [80] H.W. Kroto, K. McKay, The formation of quasi-isosahedral spiral shell carbon particles, *Nature* 331 (328) (1988), <https://doi.org/10.1038/331328a0>.
- [81] B.Y. Xia, B. Gates, Y. Yin, Y. Lu, Monodispersed colloidal spheres: old materials with new applications, *Publ. Online* (2000) 693–713.
- [82] L. Frusteri, C. Cannilla, K. Barbera, S. Perathoner, G. Centi, F. Frusteri, Carbon growth evidences as a result of benzene pyrolysis, *Carbon N. Y* 59 (2013) 296–307, <https://doi.org/10.1016/j.carbon.2013.03.022>.
- [83] Z.P. Liu, X.Q. Gong, J. Kohanoff, C. Sanchez, P. Hu, Catalytic role of metal oxides in gold-based catalysts: a first principles study of co oxidation on TiO₂supported au, *Phys. Rev. Lett.* 91 (26) (2003) 1–4, <https://doi.org/10.1103/PhysRevLett.91.266102>.
- [84] S. Manivel, L.F.A. Amirtharaj, M. Arivazhagan, B. Angle, FT-IR and FT-Raman spectra molecular geometry vibrational assignments, *First Order Hyper Polariz. HOMO-LUMO Anal. Benzyl Fluor.* e 97 (2016) 42111–42116.
- [85] C. Harris, F. Hardcastle, Bond length - bond valence relationships for carbon - carbon and carbon - oxygen bonds, *J. Ark. Acad. Sci.* (2015) 69, <https://doi.org/10.54119/jaas.2015.6905>.
- [86] F. Mouhat, F.X. Coudert, M.L. Bocquet, Structure and chemistry of graphene oxide in liquid water from first principles, *Nat. Commun.* 11 (1) (2020) 1–9, <https://doi.org/10.1038/s41467-020-15381-y>.
- [87] S. Bakhta, Z. Sadaoui, U. Lassi, H. Romar, R. Kupila, J. Vieillard, Performances of metals modified activated carbons for fluoride removal from aqueous solutions, *Chem. Phys. Lett.* 754 (June) (2020), 137705, <https://doi.org/10.1016/j.cplett.2020.137705>.
- [88] H. Arkin, W. Janke, Polymer adsorption on curved surfaces, *Phys. Rev. E* 96 (6) (2017) 12369–12375, <https://doi.org/10.1103/PhysRevE.96.062504>.